

Enhanced specular Andreev reflection in bilayer grapheneAbhiram Soori,^{1,2} Manas Ranjan Sahu,¹ Anindya Das,¹ and Subroto Mukerjee¹¹*Department of Physics, Indian Institute of Science, Bengaluru 560012, India*²*International Centre for Theoretical Sciences, Survey No. 151, Tata Institute of Fundamental Research, Shivakote, Hesarghatta Hobli, Bengaluru 560089, India*

(Received 10 January 2018; revised manuscript received 16 April 2018; published 1 August 2018)

Andreev reflection in graphene is special since it can be of two types, retro or specular. Specular Andreev reflection (SAR) dominates when the position of the Fermi energy in graphene is comparable to or smaller than the superconducting gap. Bilayer graphene (BLG) is an ideal candidate to observe the crossover from retro to specular since the Fermi energy broadening near the Dirac point is much weaker compared to monolayer graphene. Recently, the observation of signatures of SAR in BLG have been reported experimentally by looking at the enhancement of conductance at finite bias near the Dirac point. However, the signatures were not very pronounced possibly due to the participation of normal quasiparticles at bias energies close to the superconducting gap. Here, we propose a scheme to observe the features of enhanced SAR even at zero bias at a normal metal (NM)–superconductor (SC) junction on BLG. Our scheme involves applying a Zeeman field to the NM side of the NM-SC junction on BLG (making the NM ferromagnetic), which energetically separates the Dirac points for up spin and down spin. We calculate the conductance as a function of chemical potential and bias within the superconducting gap and show that well-defined regions of specular- and retro-type Andreev reflection exist. We compare the results with and without superconductivity. We also investigate the possibility of the formation of a p-n junction at the interface between the NM and SC due to a work function mismatch.

DOI: [10.1103/PhysRevB.98.075301](https://doi.org/10.1103/PhysRevB.98.075301)**I. INTRODUCTION**

Andreev reflection (AR)—a scattering process by which a current can be driven into a superconductor (SC) from a normal metal (NM) by applying a bias within the superconducting gap—was first discovered by Andreev [1] and has been extensively studied for several decades [2,3]. Graphene, on the other hand, has attracted a huge interest in the past decade owing to its electronic and material properties [4–7]. Graphene is a semimetal whose electronic structure can be described by a Dirac Hamiltonian (with a vanishingly small mass). Andreev reflection has been studied both theoretically [8–12] and experimentally [13] in graphene. What makes Andreev reflection in graphene special is that it can be of two types: one where the reflected hole retraces the path of the incident electron (called retro reflection) and another where the reflected hole moves away, not tracing back the path of the incident electron (called specular reflection) [9,13]. Specular Andreev reflection has not been observed in graphene due to charge-density fluctuations across the sample [13], but a weak qualitative agreement is observed in bilayer graphene [14,15]. Bilayer graphene (BLG) [16] is a better candidate to observe specular Andreev reflection since charge-density fluctuations are much smaller than in monolayer graphene. In the experimental setup, a part of the BLG is kept in proximity to a SC, which induces superconducting correlations on BLG. It can be seen in Fig. 3(a) of Ref. [14], which shows only a weak qualitative agreement between the experimental observations and underlying theoretical calculations (note also the very different color scales of the experimental and theoretical plots required to arrive at even this level of agreement).

Generally speaking, Andreev reflection is a process where an electron incident from a normal metal into the superconductor results in a reflected hole. This is equivalent to saying that two electrons on the normal metal side—one from above the Fermi energy and one from below the Fermi energy—pair up and go into the superconductor as a Cooper pair [2]. We use the latter convention for our analysis.

In a manner similar to that for Andreev reflection in monolayer graphene [9], retro and specular Andreev reflection can also be understood in bilayer graphene [14,15]. If both the electrons participating in the reflection come from the same side of the charge neutrality point (CNP), the Andreev reflection is of the retro type, while if the two electrons come from opposite sides of the CNP, the Andreev reflection is of the specular type. This is because the momentum of the reflected hole along the y direction has to be same as that of the incident electron. This means that when the hole originates from the same side of the CNP as that of the incident electron, the velocities along the y direction of the two electrons participating in Andreev reflection have opposite signs. On the other hand, when the hole originates from the opposite side of the CNP as that of the incident electron, the velocities along the y direction of the two electrons participating in Andreev reflection have the same sign. This is shown in Fig. 1(a).

Furthermore, the two electrons must have opposite spin. This allows us to separate the CNPs for the up-spin and the down-spin bands by applying a Zeeman field. In this work, we add a Zeeman field E_{z0} to the NM part of the NM-SC junction on BLG and calculate the conductance spectrum as a function of chemical potential and bias energy. As shown in Fig. 1(b), for small chemical potential ($|\mu| < E_{z0}$) and small

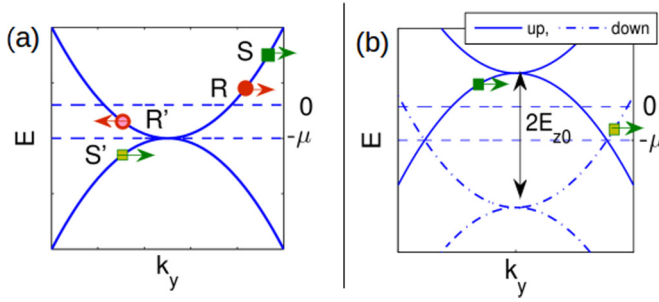


FIG. 1. The subgap band structures of the NM part of the NM-SC setup. (a) Zero Zeeman field in the NM part. The points R and R' correspond to two electrons contributing to retro Andreev reflection, while the points S and S' correspond to electrons contributing to specular Andreev reflection. (b) Finite Zeeman field E_{z0} in the NM part. The dispersion for up spin and down spin have the CNPs separated well energetically. Both the electron states shown contribute to specular Andreev reflection.

bias ($|eV_{\text{bias}}| < E_{z0} - |\mu|$) the Andreev reflection is specular. We discuss several features of the conductance spectrum in the presence of a Zeeman field, where the main highlight is the enhanced specular Andreev reflection (SAR) at zero chemical potential and zero bias energy.

The paper is organized as follows. In Sec. II, the calculation is presented. In Sec. III, we show the main results. In Sec. IV, a comparative analysis replacing the superconductor with normal metal is discussed. In Sec. V, connection to experiments is discussed. Finally, in Sec. VI, the work is summarized. In Appendix A, calculations for the system where the superconductor is replaced with normal metal are shown. In Appendix B, the system where the effect of step height is extended in the normal metal region is studied.

II. CALCULATION

The BLG Hamiltonian at either of the two degeneracy points is

$$H_0 = \hbar v(k_x \sigma_x - k_y \sigma_y \lambda_z) - t_{\perp}(\lambda_x + \lambda_x \sigma_z)/2, \quad (1)$$

where $\vec{k} = (k_x, k_y)$ is the momentum with respect to the \vec{K} point at the top layer and, for the bottom layer, $\vec{k} = (k_x, k_y)$ is the momentum with respect to \vec{K}' , v is the Fermi velocity, and t_{\perp} is the coupling between the two layers. The layer asymmetry term is absent in this Hamiltonian. The choice of basis is $[u_{A1}, u_{A2}, u_{B1}, u_{B2}]$. A and B refer to two kinds of lattice points in each layer of graphene, while 1 and 2 refer to the two layers of graphene. σ 's are the Pauli matrices in the A, B basis, while λ 's are the Pauli matrices in the 1,2 basis. This Hamiltonian can be diagonalized to get the eigenspectrum $E(\vec{k}) = v_{\sigma} \sqrt{(\hbar v \vec{k})^2 + t_{\perp}^2/2} + v_{\lambda} t_{\perp} \sqrt{(\hbar v \vec{k})^2 + t_{\perp}^2/4}$, where $v_{\lambda}, v_{\sigma} = \pm 1$. The index σ corresponds to the bipartite pseudospin in graphene and the index λ corresponds to the two layers of BLG.

The eigenvector at an energy E and momentum (k_x, k_y) is

$$\vec{u}(E, k_x) = \frac{1}{N} \begin{bmatrix} -t_{\perp} E^2 \\ [E^2 - (\hbar v \vec{k})^2] E \\ -t_{\perp} \hbar v k_{-} E \\ \hbar v k_{+} [E^2 - (\hbar v \vec{k})^2] \end{bmatrix}, \quad (2)$$

where $k_{\pm} = k_x \pm i k_y$ and N is the normalization factor for the pseudospin such that $\vec{u}^{\dagger} \vec{u} = 1$.

The Hamiltonian for the NM-SC junction on BLG is

$$H = [H_0 - \mu - U(x)] \tau_z - E_z(x) s_z + \Delta(x) \tau_x, \quad (3)$$

where $U(x) = U_0 \eta(-x)$, s_z corresponds to the real spin, $E_z(x) = E_{z0} \eta(x)$ is the Zeeman field and can be nonzero only on the NM side, $\Delta(x) = \Delta \eta(-x)$, $\eta(x)$ is the Heaviside step function, and the τ matrices act in the particle-hole sector. The wave function for an electron at energy E (in the range $|E| < \Delta \ll t_{\perp}$) and spin s ($s = \pm 1$ is the eigenvalue of the operator s_z), incident from the NM side onto the SC, has the form $\psi_s(x) e^{i k_y y}$, such that

$$\begin{aligned} \psi_s(x) = & (e^{-i k_x^e x} \vec{u}_{N,s}(\epsilon, -k_x^e) + r_N e^{i k_x^e x} \vec{u}_{N,s}(\epsilon, k_x^e)) \begin{bmatrix} 0 \\ 1 \end{bmatrix} \\ & + r_A e^{-i k_x^h x} \vec{v}_{N,s}(\epsilon_h, -k_x^h) \begin{bmatrix} 0 \\ 1 \end{bmatrix} \\ & + \tilde{r}_N e^{-\kappa x} \vec{u}_{N,s}(\epsilon, i\kappa) \begin{bmatrix} 1 \\ 0 \end{bmatrix} \\ & + \tilde{r}_A e^{-\kappa^h x} \vec{v}_{N,s}(\epsilon_h, i\kappa^h) \begin{bmatrix} 0 \\ 1 \end{bmatrix}, \quad \text{for } x > 0, \\ = & \sum_{j=1}^4 w_{j,s} e^{i k_j^s x} \vec{u}_s(k_j^S), \quad \text{for } x < 0, \end{aligned} \quad (4)$$

where $\vec{u}_{N,s}(\epsilon, k_x)$ and $\vec{v}_{N,s}(\epsilon, k_x)$ are the electron and hole sector eigenspinors of the Hamiltonian on the NM side [given by Eq. (2)] with x component of momentum k_x , and $\vec{u}_s(k_j^S)$ is the eigenspinor on the SC side with x component of momentum k_j^S ; furthermore, the x component of the electron and hole momenta on the NM side are given by

$$\begin{aligned} \hbar v k_x^e &= \text{sign}(\epsilon) \sqrt{\epsilon^2 + 2t_{\perp} |\epsilon| - (\hbar v k_y)^2}, \\ \hbar v k_x^h &= \text{sign}(\epsilon_h) \sqrt{\epsilon_h^2 + 2t_{\perp} |\epsilon_h| - (\hbar v k_y)^2}, \\ \hbar v \kappa &= \sqrt{(\hbar v k_y)^2 + 2t_{\perp} |\epsilon| - \epsilon^2}, \\ \hbar v \kappa^h &= \sqrt{(\hbar v k_y)^2 + 2t_{\perp} |\epsilon_h| - \epsilon_h^2}, \end{aligned} \quad (5)$$

where $\epsilon = (E + \mu + s E_{z0})$ and $\epsilon_h = (\mu - s E_{z0} - E)$. On the SC side, k_j^S has a nonzero imaginary part at subgap energies. The complex values of k_j^S arise as complex conjugates and thus there are eight in all. Normalizability allows only four modes (out of eight) which have a negative imaginary part. Different values of k_j^S are obtained numerically from the eigenvalue-eigenvector equation. We employ the boundary condition that the wave function is continuous at $x = 0$ to solve for the scattering coefficients.

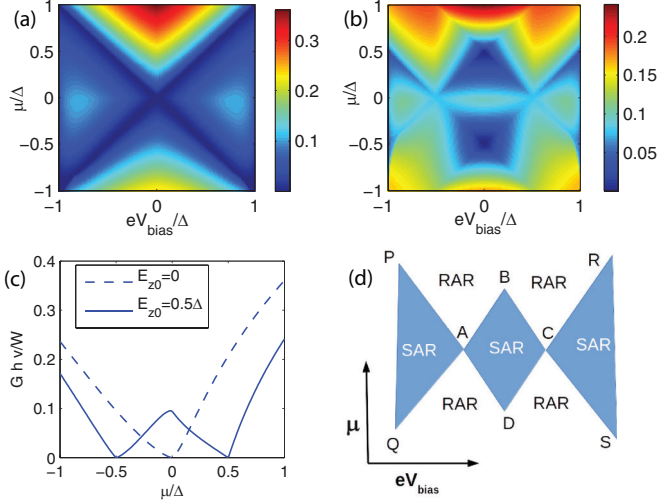


FIG. 2. (a)–(c) $G h v / W$ in units of $t_{\perp} 2e^2 / h$ is plotted. Parameters: (a) $\Delta = 0.003 t_{\perp}$, $U_0 = \Delta$, and $E_{z0} = 0$; (b) $\Delta = 0.003 t_{\perp}$, $U_0 = \Delta$, and $E_{z0} = 0.5\Delta$; and (c) $\Delta = 0.003 t_{\perp}$, $U_0 = \Delta$, and $eV_{\text{bias}} = 0$. (d) Schematic diagram showing regions of specular (SAR) and retro (RAR) Andreev reflections.

Current operator and the conductance. From the Hamiltonian, it can be shown that the current for the NM part of the BLG has the form $\vec{J}_s = e v \psi_s^{\dagger} (\sigma_x, -\sigma_y \lambda_z) \psi_s$. The differential conductance is obtained by summing over J_s for all possible values of (k_x, k_y) and $s = \pm 1$ at a given energy E such that the x component of the velocity of the incident electron points along the $-\hat{x}$ direction. We calculate the scattering amplitudes and the conductance of the junction. The cross terms ($r_N r_A$) drop out while calculating the conductance and only the terms proportional to $|r_N|^2$ and $|r_A|^2$ contribute to the current. The total current is $\vec{I} = \int dk_x \int dk_y \sum_s \vec{J}_s(k_x, k_y)$ and the only nonzero component of \vec{I} is along $-\hat{x}$ (i.e., $\vec{I} = -\hat{x} \cdot I$). We are interested in calculating the conductance $G = dI/dV$, which is given by the expression [17]

$$G = \frac{2e^2}{h} \sum_s \frac{W(\mu + sE_{z0} + E + t_{\perp}/2)}{h v} \int_{-\theta_{c,s}}^{\theta_{c,s}} d\theta \psi_s^{\dagger} \sigma_x \psi_s, \quad (6)$$

where W is the width of the bilayer graphene–superconductor interface and the factor of 2 is for valley degeneracy. The critical angle for spin s is given by $\theta_{c,s} = \sin^{-1} [\min \{(k_{h,\bar{s}}/k_{e,s}), 1\}]$ where $k_{h,\bar{s}}$ and $k_{e,s}$ are the magnitudes of the momenta \vec{k} in the hole band with spin \bar{s} and the electron band with spin s (\bar{s} is opposite to s) at energy $E = eV_{\text{bias}}$, respectively.

III. RESULTS

Results of the conductance calculation for two choices of parameters have been plotted as contour plots in Figs. 2(a) and 2(b). We discuss the features observed in the contour plots below.

Zero Zeeman field. In Fig. 2(a), a dominant feature is two dark, thick lines that appear along the diagonals: $eV_{\text{bias}} =$

$\pm\mu$. These correspond to one of the two electron Fermi surfaces participating in Andreev reflection at $eV_{\text{bias}} = \pm\mu$ having zero circumference. The lines $eV_{\text{bias}} = \pm\mu$ correspond to crossover from retro to specular Andreev reflection. Another feature is that there are two islands of light blue color around $\mu = 0$, $eV_{\text{bias}} \sim \pm 0.8\Delta$. This corresponds to specular Andreev reflection since the two electrons participating in the Andreev reflection come from above and below the CNP. All the data points in the region $|eV_{\text{bias}}| > |\mu|$ correspond to specular Andreev reflection. Similarly, all the data points in the region $|eV_{\text{bias}}| < |\mu|$ correspond to retro Andreev reflection. We also notice an asymmetry in $\mu \rightarrow -\mu$, which is due to a finite U_0 . These results and the discussion agree with that in Ref. [15].

Nonzero Zeeman field. In Fig. 2(b), the Zeeman field in the normal metal region E_{z0} is chosen to be 0.5Δ . The striking features of this contour plot are (i) three light blue islands, two of which are located around $\mu = 0$, $eV_{\text{bias}} \sim \pm 0.8\Delta$ and one located around $\mu = 0$, $eV_{\text{bias}} \sim 0$, and (ii) two dark blue patches located around $\mu = 0.5\Delta$, $eV_{\text{bias}} \sim 0$.

To understand the features of Fig. 2(b), let us define different points on the contour plot: $A = (-0.5\Delta, 0)$, $B = (0, 0.5\Delta)$, $C = (0.5\Delta, 0)$, $D = (0, -0.5\Delta)$, $P = (-\Delta, 0.5\Delta)$, $Q = (-\Delta, -0.5\Delta)$, $R = (\Delta, 0.5\Delta)$, and $S = (\Delta, -0.5\Delta)$ [each of these points is written in the form (eV_{bias}, μ)]. Now, within the diamond $ABCD$, both the electrons contributing to Andreev reflection lie on different sides of the charge neutrality point. So, Andreev reflection is specular within this diamond. Also, in the triangles PAQ and RCS the two electrons contributing to Andreev reflection lie on different sides of the CNP. Hence, Andreev reflection is specular in these regions. Outside of the two triangles and the diamond, the two electrons contributing to Andreev reflection lie on the same side of the charge neutrality point. Hence, in these regions, Andreev reflection is retro. In each of the two dark blue patches around the points B and D the data points are in proximity to CNP for both the electrons participating in the Andreev reflection. Since the size of the Fermi surface approaches zero as one tends to the CNP, the conductance is suppressed around points B and D . In contrast, along the lines PA , QA , AB , BC , CD , DA , RC , and CS away from points B and D , data points for only one of the two participating electrons (in Andreev reflection) is at the charge neutrality point.

More generally, for a given choice of E_{z0} , the diamond $ABCD$ is formed by the points $A = (-E_{z0}, 0)$, $B = (0, E_{z0})$, $C = (E_{z0}, 0)$, and $D = (0, -E_{z0})$, and the points $P = (-\Delta, \Delta - E_{z0})$, $Q = (-\Delta, -\Delta + E_{z0})$, $R = (\Delta, \Delta - E_{z0})$, and $S = (\Delta, -\Delta + E_{z0})$ form the triangles PAQ and RCS . Hence, in the case when $E_{z0} = 0$, the diamond $ABCD$ has zero area as can be seen in Fig. 2(a). And the regions inside the two triangles PAQ and RCS are described by the inequalities $-(eV_{\text{bias}} + E_{z0}) > |\mu|$ and $(eV_{\text{bias}} - E_{z0}) > |\mu|$, respectively. These are the regions where the Andreev reflection is specular. Outside these regions, the Andreev reflection is retro.

Zero-bias cuts of Figs. 2(a) and 2(b) have been plotted in Fig. 2(c). These clearly show that around the CNP, the zero-bias conductance is enhanced under an applied Zeeman field, while in the case of zero Zeeman field, the zero-bias conductance is suppressed.

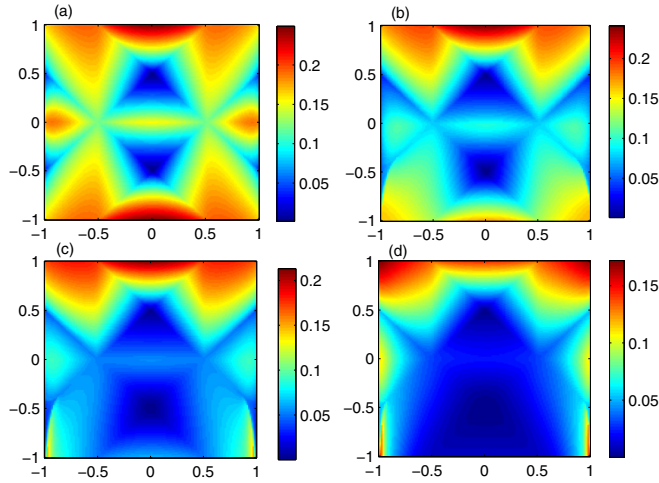


FIG. 3. Conductance spectra for the choice of parameters (a) $U_0 = 0$, (b) $U_0 = \Delta$, (c) $U_0 = 2\Delta$, and (d) $U_0 = 5\Delta$. $G\hbar v/W$ in units of $t_{\perp}2e^2/h$ is plotted. The x axis is eV_{bias}/Δ and the y axis is μ/Δ . Parameters: $\Delta = 0.003t_{\perp}$ and $E_{z0} = 0.5\Delta$.

Choice of the parameter U_0 . Previously, we chose $U_0 = \Delta$ so as to allow for significant conductance despite accounting for a work function mismatch [modeled by the step function $U(x)$]. Now, we examine the features of the conductance spectrum for different choices of U_0 and make a connection to previous works.

The step height U_0 essentially captures the junction transparency. For larger magnitudes of U_0 , the junction is less transparent and has a high resistance. We can see from Fig. 3 that for larger values of U_0 , the features of crossover from retro to specular Andreev reflection discussed earlier get blurred. From the works of Efetov *et al.* [14,15], we note that when NbSe₂ is used as the superconductor on top of the BLG, the parameters are $U_0 = 5$ meV and $\Delta = 1.2$ meV. This closely corresponds to Fig. 3(d) and we see that the features of the crossover from retro to specular Andreev reflection begin to vanish for the value of $U_0 = 5\Delta$. To see the features for higher values of U_0 , we plot the conductance on a logarithmic scale in Fig. 4. We see that the features discussed earlier vanish smoothly over the values of $U_0 = 5\Delta, 10\Delta, 100\Delta$, and t_{\perp} , except for two dips at $(eV_{\text{bias}}, \mu) = (0, \pm E_{z0})$. However, the dips correspond to orders-of-magnitude-smaller conductance. Thus, we find that a transparent junction is very crucial to observing the features of crossover from retro to specular Andreev reflection.

IV. COMPARATIVE ANALYSIS OF THE RESULTS REPLACING THE SUPERCONDUCTOR WITH NORMAL METAL

In this section, we discuss the results of the system where superconductivity in the system is absent and make comparison to the results with the system containing superconductivity. We denote the part of the system having a nonzero Zeeman field by F (ferromagnet), and N refers to the normal metal part which has no Zeeman field. $\Delta(x) = 0$ for all x in the NF junction. The calculation for the NF junction is presented in Appendix A. As can be seen from the calculations, the

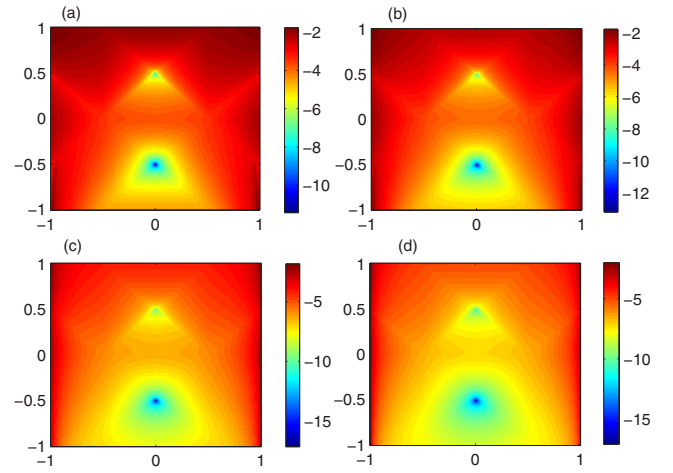


FIG. 4. Conductance spectra on a logarithmic scale for the choice of parameters (a) $U_0 = 5\Delta$, (b) $U_0 = 10\Delta$, (c) $U_0 = 100\Delta$, and (d) $U_0 = t_{\perp}$. $\log[G\hbar^2v/(Wt_{\perp}2e^2)]$ is plotted. The x axis is eV_{bias}/Δ and the y axis is μ/Δ . Parameters: $\Delta = 0.003t_{\perp}$ and $E_{z0} = 0.5\Delta$.

bias eV_{bias} and the chemical potential μ enter the equations as $(eV_{\text{bias}} + \mu)$. Hence, the conductance depends only on the linear combination $(eV_{\text{bias}} + \mu)$ in the contour plot which is apparent in Fig. 5.

In Fig. 6, the conductance is plotted as a function of $(eV_{\text{bias}} + \mu)$, for different values of step height U_0 . For $U_0 = 0$, the conductance goes to zero at $(\mu + eV_{\text{bias}}) = 0$, since the size of the Fermi surface on the normal metal side goes to zero, and there are no momentum modes to carry the current. For finite values of U_0 , the situation changes since at $(eV_{\text{bias}} + \mu) = 0$ the Fermi surface has a finite size, and the current can flow from the F side to the N side. The asymmetry around $(\mu + eV_{\text{bias}}) = 0$ is because of a finite value of U_0 .

Now, we turn to the comparison of conductances of different systems (NN, NF, SN, and SF) for a given choice of U_0 and other parameters. For $U_0 = 0$ (Fig. 7, top), all the curves are symmetric, while for $U_0 = \Delta$ the curves are not symmetric (except for SN and SF). For SF, the minima at $eV_{\text{bias}} = \pm E_{z0}$ and maximum at $eV_{\text{bias}} = 0$ are due to the dispersions displaced due to Zeeman fields. This bump is where the specular Andreev reflection is enhanced by the Zeeman field. For NN, NF, and SN in the case $U_0 = 0$, the conductance is zero at $eV_{\text{bias}} = 0$, which is due to zero size of the Fermi surface of the N region. When $U_0 = \Delta$ (see Fig. 7, bottom), the size of Fermi surface is nonzero in the N region to the left in the NN and

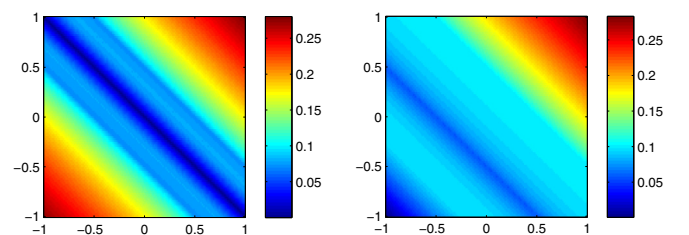


FIG. 5. Conductance spectra $G\hbar v/W$ in units of $t_{\perp}2e^2/h$ for NF junction. Left, $U = 0$; right, $U = 2\Delta$. The x axis is eV_{bias}/Δ and the y axis is μ/Δ . For both, $\Delta = 0.003t_{\perp}$ and $E_{z0} = 0.5\Delta$.

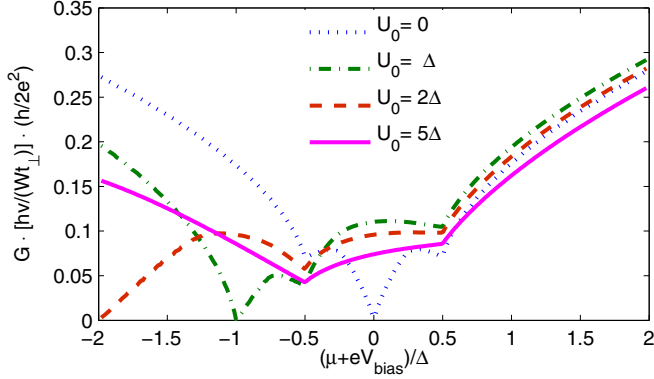


FIG. 6. Conductance of NF junction, for different values of the step height U_0 . Parameters: $E_{z0} = 0.5\Delta$, and $(eV_{\text{bias}} - \mu) = 0$, where $\Delta = 0.003t_{\perp}$.

NF configurations, and there is a finite conductance even at $eV_{\text{bias}} = 0$ for the NF configuration.

Now, we compare different curves in the bottom panel of Fig. 7. For NN and SN configurations, the N region for $x > 0$ has zero-sized Fermi surface at zero bias. Hence the conductance at zero bias is zero (despite a non-zero-sized Fermi surface in the region $x < 0$ for NN). Now, when we

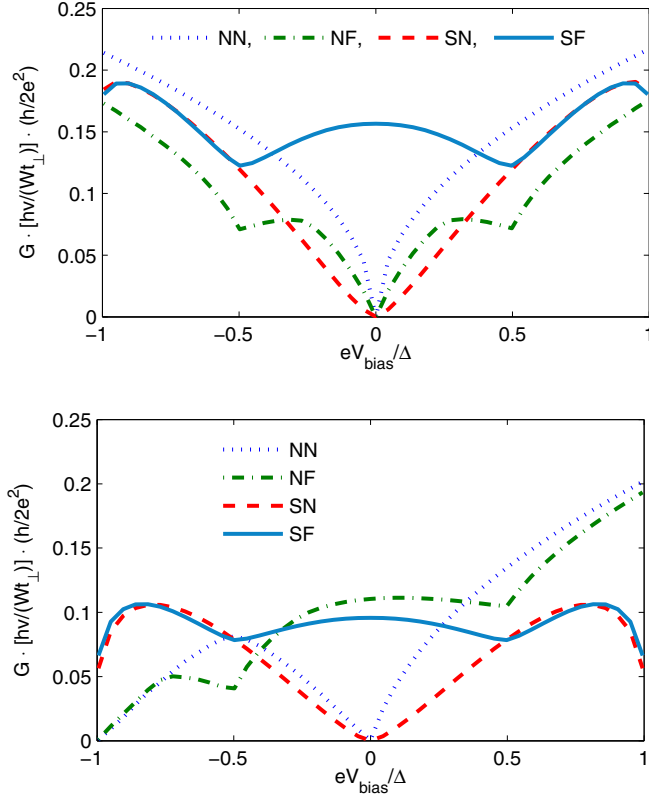


FIG. 7. Conductance Ghv/W in units of $t_{\perp}2e^2/h$ is plotted for different configurations of the setup: normal-normal (NN), normal-ferromagnet (NF), superconductor-normal (SN), and superconductor-ferromagnet (SF). See text for further information. Top, $U_0 = 0$; bottom, $U_0 = \Delta$. Parameters: $E_{z0} = 0.5\Delta$ (for F), where $\Delta = 0.003t_{\perp}$ and $\mu = 0$ (for all curves).

turn to the case of NF, the Fermi surfaces on both sides of the junction at $eV_{\text{bias}} = 0$ have nonzero size. Hence, the conductance is finite around $eV_{\text{bias}} = 0$. The conductance for NF approaches zero as $eV_{\text{bias}} \rightarrow \Delta$ since the size of the Fermi surface approaches zero on the N side of the junction as we have chosen $U_0 = \Delta$. For the case of SF, the conductance is nonzero in the entire range shown since the size of the Fermi surface on the F side is always nonzero due to a finite value of the Zeeman field ($E_{z0} = 0.5\Delta$), and on the S side there is superconducting gap which favors Andreev reflection. Finally, the conductances in the lower panel are smaller than those in the upper panel since the step height U_0 is zero in the upper panel and Δ in the lower panel, reducing the transparency of the junctions studied in the lower panel.

V. EXPERIMENTAL RELEVANCE

To implement our scheme experimentally, it is important to apply a Zeeman field in the NM part of the junction. An in-plane magnetic field which is less than the critical field to kill the superconductivity of the SC part in the system will achieve this. Another way to implement a Zeeman field is to bring a ferromagnetic insulator in proximity to the NM side of the junction. It has been shown that ferromagnetism can be induced in graphene by such proximity coupling with several materials such as EuO, YIG, and EuS [18–20].

A typical sample will have a disorder which manifests as Fermi energy broadening $\delta\epsilon_F$. This means that the BLG sample must be of a sufficiently high quality so that the Fermi energy broadening $\delta\epsilon_F$ is small ($\delta\epsilon_F \ll \Delta$). Furthermore, observing the features of crossover for a fixed bias $eV_{\text{bias}} \ll \Delta$ as μ is varied is important as the quasiparticle contribution to transport is the least in this regime. In addition, a finite temperature will result in thermal broadening; hence, performing the experiment at a low temperature is necessary to observe the features discussed here. The temperature has to be low compared to both the superconducting gap (~ 14 K in NbSe₂ [14]) and Zeeman energy (~ 10 K). Experimentally, reaching temperatures of about 100 mK is possible and hence temperature does not pose a hindrance to implementing our scheme in realistic systems.

In a realistic system, the work function mismatch between the NM and SC regions can result in the formation of a NM region having a length scale a at the interface as discussed in Ref. [21]. Also, from the value of the work functions of NbSe₂ and BLG, the step height U_0 is chosen to be $1\text{eV} > t_{\perp}$ in Ref. [21] in contrast to the limit $U_0 \ll t_{\perp}$ in Refs. [14,15], where the value of U_0 is chosen to match the experimental results. Our calculations combined with the choice of U_0 in Refs. [14,15] point to a small value of a ($a \ll 100$ nm) in contrast to the assertion made in Ref. [21]. This means that the effects of a p-n junction formed at the NM-SC interface may be negligible. In Appendix B, we study the effect of having a finite a and show that it can be negligible.

VI. SUMMARY AND CONCLUSION

We have studied Andreev reflection at a junction of bilayer graphene and a superconductor. Since our main objective has been to observe the enhanced signatures of specular Andreev reflection, we introduce a Zeeman field and study the features

on a contour plot of conductance versus chemical potential and bias voltage when these two energy scales are less than the superconducting gap. We find that a finite Zeeman field produces a diamond-shaped region at the center where the Andreev reflection is purely specular. Furthermore, the lines bordering the diamond-shaped region and two patches around the low-bias region at the corners of the diamond show a low conductance, where the crossover from specular- to retro-type Andreev reflection occurs. Importantly, we find that for a barrier step height that is of the same order of magnitude as the superconducting gap, the features of the crossover from retro to specular Andreev reflection are observable and for a barrier step height much larger than the superconducting gap, the features vanish except for small regions of low conductance at $(eV_{\text{bias}}, \mu) = (0, \pm E_{z0})$. We have also analyzed the relative contributions from normal-state conductance, where the superconductivity is switched off. Furthermore, we have discussed how our calculations can be tested in an experimental system.

ACKNOWLEDGMENTS

A.S. thanks Nanomission, Department of Science and Technology (DST) for the financial support under Grants No. DSTO1470 and No. DSTO1597. A.S. thanks DST Nanomission (DSTO1597) for funding. S.M. thanks the Indo-Israeli UGC-ISF project for funding.

APPENDIX A

In this section, we give details of the calculation for the system comprising a Zeeman-field-induced ferromagnetic region in contact with the normal metal region. This is simply the limit of the NM-SC junction described by Eq. (3) where $\Delta(x) = 0$ for all x . The wave function for an electron incident on the junction from $x > 0$ onto $x < 0$, with energy E , has the form $\phi_s(x)e^{ik_y y}$, where

$$\begin{aligned} \phi_s(x) &= e^{-ik_x^e x} \vec{u}_{N,s}(\epsilon, -k_x^e) + r_N e^{ik_x^e x} \vec{u}_{N,s}(\epsilon, k_x^e) \\ &\quad + \tilde{r}_N e^{-\kappa x} \vec{u}_{N,s}(\epsilon, i\kappa), \quad \text{for } x > 0, \\ &= t_N e^{-i\tilde{k}_x^e x} \vec{u}_{N,s}(\tilde{\epsilon}, -\tilde{k}_x^e) + \tilde{t}_N e^{\tilde{\kappa} x} \vec{u}_{N,s}(\tilde{\epsilon}, -i\tilde{\kappa}) \\ &\quad \text{for } x < 0. \end{aligned} \quad (\text{A1})$$

Here, $\epsilon = E + \mu + sE_{z0}$, $\tilde{\epsilon} = E + \mu + U_0$, $k_y = \sqrt{\epsilon^2 + t_{\perp}|\epsilon|} \sin \theta / (\hbar v)$ (θ is the angle of incidence so that the normal incidence corresponds to $\theta = 0$),

$$\begin{aligned} k_x^e &= \text{sign}(\epsilon) \sqrt{\epsilon^2 + t_{\perp}|\epsilon| - (\hbar v k_y)^2} / (\hbar v), \\ \kappa &= \sqrt{(\hbar v k_y)^2 + t_{\perp}|\epsilon| - \epsilon^2} / (\hbar v), \\ \tilde{k}_x^e &= \text{sign}(\tilde{\epsilon}) \sqrt{\tilde{\epsilon}^2 + t_{\perp}|\tilde{\epsilon}| - (\hbar v k_y)^2} / (\hbar v), \\ \text{and } \tilde{\kappa} &= \sqrt{(\hbar v k_y)^2 + t_{\perp}|\tilde{\epsilon}| - \tilde{\epsilon}^2} / (\hbar v). \end{aligned} \quad (\text{A2})$$

Now, using the boundary condition, which is continuity of the wave function at $x = 0$, one can determine the scattering amplitudes r_N , \tilde{r}_N , t_N , and \tilde{t}_N . With this, the wave function is determined and, using a formula similar to Eq. (6), the conductance can be calculated.

APPENDIX B

In this part, we study the effect of having a finite region of length a on the NM part of the junction where $U(x) \neq 0$. The Hamiltonian has the same form as in Eq. (3), except for two changes: $U(x) = U_0 \eta(a - x)$ and $E_z(x) = E_{z0} \eta(x - a)$, where $\eta(x)$ is a Heaviside step function. The wave function for an electron at energy E (in the range $|E| < \Delta \ll t_{\perp}$) and spin s ($s = \pm 1$ is the eigenvalue of the operator s_z), incident from the NM side onto the SC, has the form $\psi_s(x)e^{ik_y y}$, such that

$$\begin{aligned} \psi_s(x) &= (e^{-ik_x^e x} \vec{u}_{N,s}(\epsilon, -k_x^e) + r_N e^{ik_x^e x} \vec{u}_{N,s}(\epsilon, k_x^e)) \begin{bmatrix} 1 \\ 0 \end{bmatrix} \\ &\quad + r_A e^{-ik_x^h x} \vec{v}_{N,s}(\epsilon_h, -k_x^h) \begin{bmatrix} 0 \\ 1 \end{bmatrix} + \tilde{r}_N e^{-\kappa x} \vec{u}_{N,s}(\epsilon, i\kappa) \begin{bmatrix} 1 \\ 0 \end{bmatrix} \\ &\quad + \tilde{r}_A e^{-\kappa x} \vec{v}_{N,s}(\epsilon_h, i\kappa^h) \begin{bmatrix} 0 \\ 1 \end{bmatrix}, \quad \text{for } x > a, \\ &= (s_{e-} e^{-ik_x^{e'} x} \vec{u}_{N',s}(\epsilon', -k_x^{e'}) + s_{e+} e^{ik_x^{e'} x} \vec{u}_{N',s}(\epsilon', k_x^{e'})) \begin{bmatrix} 1 \\ 0 \end{bmatrix} \\ &\quad + (s_{h-} e^{-ik_x^{h'} x} \vec{v}_{N',s}(\epsilon', -k_x^{h'})) \\ &\quad + s_{h+} e^{ik_x^{h'} x} \vec{v}_{N',s}(\epsilon', k_x^{h'})) \begin{bmatrix} 0 \\ 1 \end{bmatrix} \\ &\quad + (\tilde{s}_{e-} e^{-\kappa_x^{e'} x} \vec{u}_{N',s}(\epsilon', i\kappa_x^{e'})) \\ &\quad + \tilde{s}_{e+} e^{\kappa_x^{e'} x} \vec{u}_{N',s}(\epsilon', -i\kappa_x^{e'})) \begin{bmatrix} 1 \\ 0 \end{bmatrix} \\ &\quad + (\tilde{s}_{h-} e^{-\kappa_x^{h'} x} \vec{v}_{N',s}(\epsilon', i\kappa_x^{h'})) \\ &\quad + \tilde{s}_{h+} e^{\kappa_x^{h'} x} \vec{v}_{N',s}(\epsilon', -i\kappa_x^{h'})) \begin{bmatrix} 0 \\ 1 \end{bmatrix}, \quad \text{for } 0 < x < a, \\ &= \sum_{j=1}^4 w_{j,s} e^{ik_j^s x} \vec{u}_s(k_j^s), \quad \text{for } x < 0, \end{aligned} \quad (\text{B1})$$

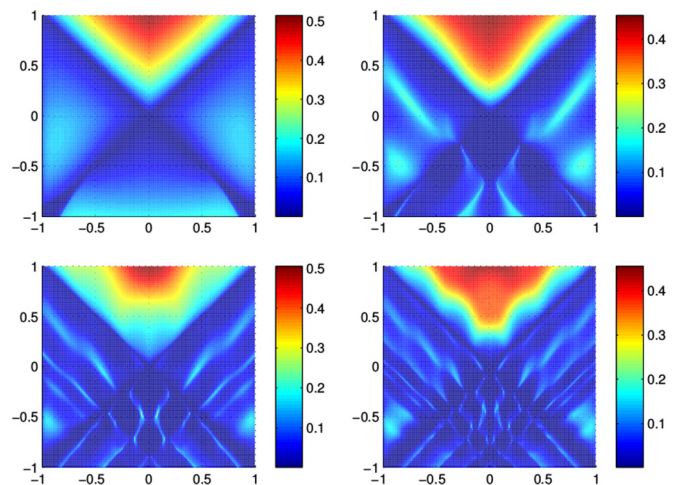


FIG. 8. Conductance spectra for the choice of parameters $a = 10, 50, 100, 150$ (in units of $\hbar v / t_{\perp}$) for top-left, top-right, bottom-left, bottom-right respectively. x -axis is eV_{bias}/Δ and y -axis is μ/Δ . Parameters: $\Delta = 0.003t_{\perp}$, $U_0 = \Delta$ and $E_{z0} = 0$.

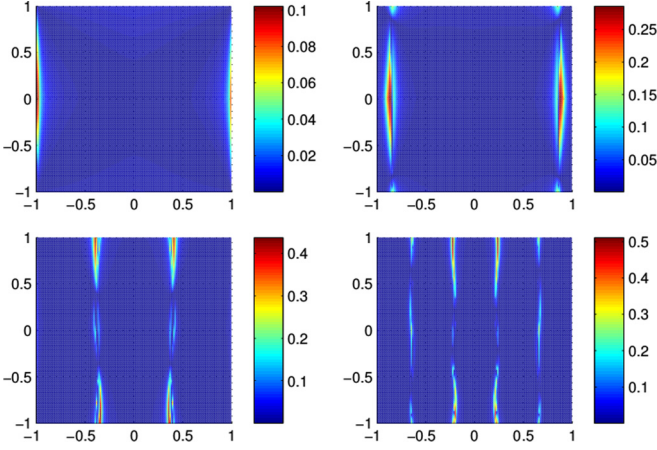


FIG. 9. Conductance spectra for the choice of parameters $a = 10, 100, 500,$ and 1000 (in units of $\hbar v/t_{\perp}$) for top left, top right, bottom left, and bottom right panels, respectively. The x axis is eV_{bias}/Δ and the y axis is μ/Δ . Parameters: $\Delta = 0.003t_{\perp}$, $U_0 = 5t_{\perp}$, and $E_{z_0} = 0$.

where $\vec{u}_{N,s}(\tilde{\epsilon}, k_x)$ and $\vec{v}_{N,s}(\tilde{\epsilon}, k_x)$ are the electron- and hole-sector eigenspinors of the Hamiltonian on the NM side [given by Eq. (2)] with x component of momentum k_x , and $\vec{u}_S(k_x^S)$ is the eigenspinor on the SC side with x component of momentum k_x^S . Furthermore, the x component of electron and hole momenta on the NM side are given by

$$\begin{aligned}
 \hbar v k_x^e &= \text{sign}(\epsilon) \sqrt{\epsilon^2 + t_{\perp} |\epsilon| - (\hbar v k_y)^2}, \\
 \hbar v k_x^h &= \text{sign}(\epsilon_h) \sqrt{\epsilon_h^2 + t_{\perp} |\epsilon_h| - (\hbar v k_y)^2}, \\
 \hbar v \kappa &= \sqrt{(\hbar v k_y)^2 + t_{\perp} |\epsilon| - \epsilon^2}, \\
 \hbar v \kappa^h &= \sqrt{(\hbar v k_y)^2 + t_{\perp} |\epsilon_h| - \epsilon_h^2}, \\
 \hbar v k_x^{e'} &= \text{sign}(\epsilon') \sqrt{\epsilon'^2 + t_{\perp} |\epsilon'| - (\hbar v k_y)^2}, \\
 \hbar v k_x^{h'} &= \text{sign}(\epsilon'_h) \sqrt{\epsilon'_h{}^2 + t_{\perp} |\epsilon'_h| - (\hbar v k_y)^2}, \\
 \hbar v \kappa^{e'} &= \sqrt{(\hbar v k_y)^2 + t_{\perp} |\epsilon'| - \epsilon'^2}, \\
 \hbar v \kappa^{h'} &= \sqrt{(\hbar v k_y)^2 + t_{\perp} |\epsilon'_h| - \epsilon'_h{}^2},
 \end{aligned} \tag{B2}$$

where $\epsilon = (E + \mu + sE_{z_0})$, $\epsilon_h = (\mu - sE_{z_0} - E)$, $\epsilon' = (E + \mu + U_0)$, and $\epsilon'_h = (\mu + U_0 - E)$. The continuity of $\psi_s(x)$ at $x = 0$ and $x = a$ in total give 16 equations for 16 scattering amplitudes to be solved. Then, the conductance is calculated using Eq. (6).

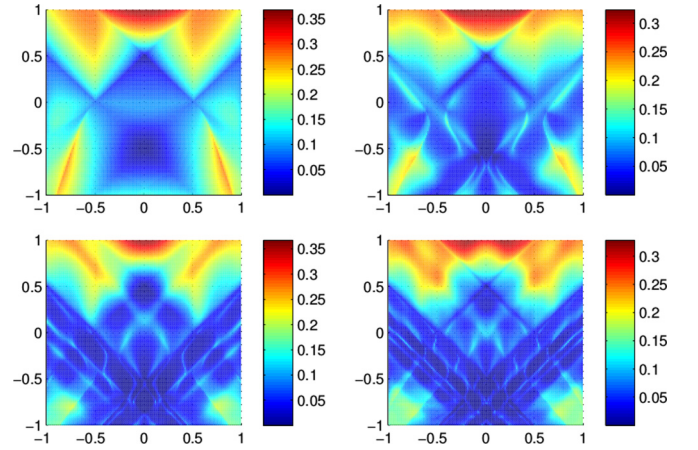


FIG. 10. Conductance spectra for the choice of parameters $a = 10, 50, 100,$ and 150 (in units of $\hbar v/t_{\perp}$) for top left, top right, bottom left, and bottom right panels, respectively. The x axis is eV_{bias}/Δ and the y axis is μ/Δ . Parameters: $\Delta = 0.003t_{\perp}$, $U_0 = \Delta$, and $E_{z_0} = 0.5\Delta$.

First, the conductance is calculated for $E_{z_0} = 0$, for various values of a and a fixed value of $U_0 = \Delta$ in Fig. 8. It can be seen that for higher values of a , Fabry-Pérot-type oscillations [22] are observed in the conductance spectra. Comparing this with the experimental results in Ref. [14], the absence of conductance oscillations there suggests that in a realistic system, a is small ($a \ll 50\hbar v/t_{\perp}$).

Next, we study the case of $U_0 = 5t_{\perp}$ (discussed in Ref. [21]), keeping $E_{z_0} = 0$ in Fig. 9 for different values of a . We see that for larger values of a ($a > 100\hbar v/t_{\perp}$), there are Fabry-Pérot-type oscillations in conductance. Comparing these with the experimental results in Ref. [14], we see that a must be small ($a \ll 100\hbar v/t_{\perp}$). While the precise values of U_0 and a are unknown in a realistic system, our results suggest that $U_0 \sim \Delta$ and $a \lesssim 10\hbar v/t_{\perp}$. Furthermore, this limit of U_0 and a is important to observe the features of the crossover from retro to specular Andreev reflection in a system with finite E_{z_0} .

Now, we turn to the case of $E_{z_0} = 0.5\Delta$. In Fig. 10, we see how the conductance spectrum changes as a is changed, keeping $U_0 = \Delta$ fixed. The features of crossover still remain, but there are oscillations in the conductance spectrum due to Fabry-Pérot-type interference, which occur due to modes in the region $0 < x < a$. The two dark regions of low conductance around the points B and D , and the dark lines PD and DS , remain. Furthermore, the dark lines BA and BC remain, while the dark lines along AQ and CS vanish. It is not possible to distinguish the Fabry-Pérot oscillations in the conductance spectrum from the crossover from specular to retro Andreev reflection, but with a knowledge of E_{z_0} and Δ the points $P, Q, R, S, A, B, C,$ and D in the conductance spectrum can be identified, thereby finding the crossover lines.

- [1] A. F. Andreev, The thermal conductivity of the intermediate state in superconductors, *J. Exp. Theor. Phys.* **19**, 1228 (1964).
 [2] G. E. Blonder, M. Tinkham, and T. M. Klapwijk, Transition from metallic to tunneling regimes in superconducting

- microconstrictions: Excess current, charge imbalance, and supercurrent conversion, *Phys. Rev. B* **25**, 4515 (1982).
 [3] A. Kastalsky, A. W. Kleinsasser, L. H. Greene, R. Bhat, F. P. Milliken, and J. P. Harbison, Observation of Pair Currents in

- Superconductor-Semiconductor Contacts, *Phys. Rev. Lett.* **67**, 3026 (1991).
- [4] K. S. Novoselov, A. K. Geim, S. V. Morozov, D. Jiang, Y. Zhang, S. V. Dubonos, I. V. Grigorieva, and A. A. Firsov, Electric field effect in atomically thin carbon films, *Science* **306**, 666 (2004).
- [5] A. H. Castro Neto, F. Guinea, N. M. R. Peres, K. S. Novoselov, and A. K. Geim, The electronic properties of graphene, *Rev. Mod. Phys.* **81**, 109 (2009).
- [6] A. V. Rozhkov, A. O. Sboychakov, A. L. Rakhmanov, and F. Nori, Electronic properties of graphene-based bilayer systems, *Phys. Rep.* **648**, 1 (2016).
- [7] E. McCann and M. Koshino, The electronic properties of bilayer graphene, *Rep. Prog. Phys.* **76**, 056503 (2013).
- [8] S. Bhattacharjee and K. Sengupta, Tunneling Conductance of Graphene NIS Junctions, *Phys. Rev. Lett.* **97**, 217001 (2006).
- [9] C. W. J. Beenakker, Specular Andreev Reflection in Graphene, *Phys. Rev. Lett.* **97**, 067007 (2006).
- [10] C. Benjamin and J. K. Pachos, Detecting entangled states in graphene via crossed Andreev reflection, *Phys. Rev. B* **78**, 235403 (2008).
- [11] L. Majidi, and M. Zareyan, Enhanced Andreev reflection in gapped graphene, *Phys. Rev. B* **86**, 075443 (2012).
- [12] D. Rainis, F. Taddei, F. Dolcini, M. Polini, and R. Fazio, Andreev reflection in graphene nanoribbons, *Phys. Rev. B* **79**, 115131 (2009).
- [13] M. R. Sahu, P. Raychaudhuri, and A. Das, Andreev reflection near the Dirac point at graphene-NbSe₂ junction, *Phys. Rev. B* **94**, 235451 (2016).
- [14] D. K. Efetov, L. Wang, C. Handschin, K. B. Efetov, J. Shuang, R. Cava, T. Taniguchi, K. Watanabe, J. Hone, C. R. Dean, and P. Kim, Specular interband Andreev reflections at van der Waals interfaces between graphene and NbSe₂, *Nat. Phys.* **12**, 328 (2016).
- [15] D. K. Efetov and K. B. Efetov, Cross-over from retro to specular Andreev reflections in bilayer graphene, *Phys. Rev. B* **94**, 075403 (2016).
- [16] T. Ludwig, Andreev reflection in bilayer graphene, *Phys. Rev. B* **75**, 195322 (2007).
- [17] R. Landauer, Spatial variation of currents and fields due to localized scatterers in metallic conduction, *IBM J. Res. Dev.* **1**, 223 (1957); Electrical resistance of disordered one-dimensional lattices, *Philos. Mag.* **21**, 863 (1970); M. Büttiker, Y. Imry, R. Landauer, and S. Pinhas, Generalized many-channel conductance formula with application to small rings, *Phys. Rev. B* **31**, 6207 (1985); M. Büttiker, Four-Terminal Phase-Coherent Conductance, *Phys. Rev. Lett.* **57**, 1761 (1986); S. Datta, *Electronic Transport in Mesoscopic Systems* (Cambridge University Press, Cambridge, U.K., 1995).
- [18] H. Haugen, D. Huertas-Hernando, and A. Brataas, Spin transport in proximity-induced ferromagnetic graphene, *Phys. Rev. B* **77**, 115406 (2008).
- [19] Z. Wang, C. Tang, R. Sachs, Y. Barlas, and J. Shi, Proximity-Induced Ferromagnetism in Graphene Revealed by the Anomalous Hall Effect, *Phys. Rev. Lett.* **114**, 016603 (2015).
- [20] P. Wei, S. Lee, F. Lemaitre, L. Pinel, D. Cutaia, W. Cha, F. Katmis, Y. Zhu, D. Heiman, J. Hone, J. S. Moodera and C.-T. Chen, Strong interfacial exchange field in the graphene/EuS heterostructure, *Nat. Mater.* **15**, 711 (2016).
- [21] Y. Takane, K. Yarimizu, and A. Kanda, Andreev reflection in a bilayer graphene junction: Role of spatial variation of the charge neutrality point, *J. Phys. Soc. Jpn.* **86**, 064707 (2017).
- [22] A. Soori, S. Das, and S. Rao, Magnetic-field-induced Fabry-Pérot resonances in helical edge states, *Phys. Rev. B* **86**, 125312 (2012).